Correction of the SMAP Sea Surface Brightness Temperature and Retrieval of Sea Surface Salinity Incorporating CYGNSS Observables

Zheng Li [ID], Fei Guo [ID], Zhiyu Zhang [ID], and Xiaohong Zhang [ID]

Abstract—The correction of sea surface brightness temperature is crucial for improving the accuracy of sea surface salinity (SSS) retrieval by L-band microwave radiometer. However, the traditional method of correcting brightness temperature using only wind speed and significant wave height (SWH) is inadequate, as sea surface roughness is affected by multiple factors. The Global Navigation Satellite System Reflectometer (GNSS-R) observables, which directly respond to sea surface roughness, have been preliminarily validated in ground-based experiments for their potential to correct sea surface brightness temperature. Compared with ground-based GNSS-R, spaceborne GNSS-R has a wider coverage and can better support the brightness temperature correction of spaceborne L-band microwave radiometers. This article has preliminarily verified the correlation between cyclone GNSS (CYGNSS) observables and brightness temperature variations, and found that the incidence angle of the observable needs to be taken into account when retrieving SSS jointly with soil moisture active and passive (SMAP) and CYGNSS. A multilayer perceptron (MLP) model was established to assess the SSS retrieval performance of SMAP combined with different parameters. The results show that the retrieval performance based on the MLP model is better than that based on the geophysical model function model. Compared with joint wind speed and SWH, joint CYGNSS observables performs better in retrieving SSS. The root mean square error of retrieval salinity decreased from 0.58 to 0.46 psu, and the correlation coefficient (R) increased from 0.83 to 0.90. This provides reference for future joint retrieval of SSS using L-band microwave radiometers and spaceborne GNSS-R.

Index Terms—Brightness temperature, cyclone Global Navigation Satellite System (CYGNSS), Global Navigation Satellite System Reflectometer (GNSS-R), sea surface salinity (SSS), soil moisture active and passive (SMAP).

Zheng Li, Fei Guo, and Zhiyu Zhang are with the School of Geodesy and Geomatics, Hubei Luojia Laboratory, Wuhan University, Wuhan 430079, China (e-mail: zheng_li@whu.edu.cn; fguo@whu.edu.cn; zyzhang_sgg@whu.edu.cn).

Xiaohong Zhang is with the School of Geodesy and Geomatics, Hubei Luojia Laboratory, Wuhan University, Wuhan 430079, China, also with the Key Laboratory of Geospace Environment and Geodesy, Ministry of Education, Wuhan 430079, China, and also with the Collaborative Innovation Center for Geospatial Technology, Wuhan University, Wuhan 430079, China (e-mail: xhzhang@sgg.whu.edu.cn).

Digital Object Identifier 10.1109/JSTARS.2023.3348880

I. INTRODUCTION

SEA surface salinity (SSS) holds significant significance within the realm of oceanography and climatology, assuming a pivotal function in comprehending climate variability, water circulation dynamics, and the intricate biogeochemical processes occurring in the oceanic domain [1], [2]. There are two main methods for measuring SSS. One is to use a floating buoy with a high-precision salinity sensor to directly measure the salinity of seawater [3]. However, this method is limited in its ability to measure large areas and provide high temporal resolution. An alternative approach involves the utilization of an L-band microwave radiometer aboard a satellite, offering comprehensive global measurements of SSS. This technique is widely regarded as the most effective method for remote sensing of SSS. Missions, such as the European Space Agency's Soil Moisture and Ocean Salinity (SMOS) [4] and NASA/CONAE's Aquarius, and Soil Moisture Active and Passive (SMAP) [5], [6], have successfully retrieved global SSS using this technology. However, unlike buoy measurements, the microwave radiometer measures the brightness temperature of the rough sea surface. To derive SSS, it is necessary to exclude factors that affect sea surface roughness and obtain the brightness temperature of the flat sea surface [7]. Therefore, the correction of the brightness temperature is key to obtaining high-precision ocean salinity products [8]. Currently, sea surface wind speed (WS) and significant wave height (SWH) are typically used to correct the brightness temperature [9]. However, sea-state corrections parameterized solely in terms of WS and/or SWH have been found to be insufficient. These parameters alone cannot fully describe the complexity of sea surface roughness [10]. Factors, such as foam and marine organisms, also influence the sea surface roughness, which leads to errors in the retrieved SSS products [11].

The emergence of Global Navigation Satellite System Reflectometer (GNSS-R) technology provides a new means for sea surface brightness temperature correction and salinity retrieval. In 1988, the utilization of GNSS-R technology for measuring sea surface scattering was initially proposed by Hall and Cordy [12]. Subsequently, GNSS-R was used for sea surface altimetry [13]. In 2000, Zavorotn and Voronovich [14] established a model for the relationship between GNSS reflection signals and sea surface roughness. Drawing upon this model, the application of GNSS-R technology has commenced for monitoring environmental

characteristics within the realms of both oceans and land [15]. This encompasses the measurement of ocean WS [16], [17], SWH [18], [19], and soil moisture [20], [21], showcasing exceptional performance. Sea surface roughness directly affects GNSS-R observations. Variations in sea surface roughness due to factors, such as wind or other environmental conditions, are reflected in GNSS-R observations [22], [23]. In 2004, Camp [24] proposed the utilization of GNSS-R for assessing sea state and correcting L-band brightness temperature variations associated with it. This idea was validated during the "Advanced L-BAnd emissiviTy and Reflectivity Observations of the Sea Surface" field experiment conducted between 2008 and 2009 [25], [26]. Based on the experimental data, an empirical relationship was established between the measured brightness temperature variations due to sea state effects and direct GNSS-R observables [27]. These results demonstrated the significant potential of GNSS-R to make necessary corrections in future salinity missions. In 2021, the cyclone GNSS (CYGNSS) L2-level WS data was used for the first time to correct the sea surface brightness temperature in SMAP and obtained SSS products with accuracy comparable to that of SMAP, demonstrating the potential of CYGNSS in SSS retrieval [28].

However, when compared with the CYGNSS WS data, CYGNSS observables exhibit a more direct response to sea surface roughness. This means that it will contribute more to the correction of brightness temperature. Therefore, this study demonstrates the feasibility of correcting the brightness temperature and retrieving SSS using the CYGNSS L1-level observables for the first time. The results indicate that more accurate SSS can be obtained by correcting sea surface brightness temperature using the CYGNSS observables compared with WS and SWH. The rest of this article is organized as follows. Section II introduces the experimental datasets and the preprocessing of the data. Section III analyzes the sensitivity of CYGNSS observables to sea surface brightness temperature variations. Section IV evaluated the SSS retrieval performance of the SMAP mission with the inclusion of CYGNSS observables. Section V discusses the potential effects of land contamination and rainfall on SSS retrieval. Finally, Section VI concludes this article.

II. DATASETS AND DATA PREPROCESSING

A. Datasets

1) CYGNSS Data: CYGNSS uses a constellation of eight satellites to receive reflected signals over tropical ocean, with an average revisit time of 7.2 h and a spatial resolution of approximately 25 km [29], [30]. This study utilized CYGNSS L1 level 3.1 version data from July 2019 to June 2022.

2) SMAP Data: The SMAP satellite is able to cover the entire globe in about 3 days with its 1000 km swath, although its orbit repeat cycle is precisely 8 days. The onboard instruments consist of a highly sensitive 1.41 GHz L-band radiometer and a complementary 1.26 GHz L-band radar sensor [31]. This study utilized SMAP SSS data (L2, v5.0) covering the period from July 2019 to June 2022.

3) Argo Data: Argo uses autonomous floats to collect temperature, salinity, and current data in ice-free oceans. With a network of over 3000 floats, Argo provides global ocean temperature and salinity profiles, with a salinity accuracy of 0.01 psu. In this study, the salinity measurement taken at a depth of approximately 5 m serves as the reference ground truth [32].

4) Sea Surface Wind Field and Temperature Data: Two WS data are used in this study, one is the WS data from National Center for Environmental Prediction (NCEP), which is the WS data used in the SMAP salinity product with a spatial resolution of 0.25°. The other is the WS data from CYGNSS L2 level version 3.1 data with a spatial resolution of 25 km. In addition, a number of other sea state parameters were used in this study, including sea surface wind direction (WD) data from NCEP, SWH data from ERA5 (the fifth generation of European Center for Medium-Range Weather Forecasts atmospheric reanalysis of the global climate), and sea surface temperature (SST) data from the Canadian Meteorological Center (CMC). The spatial resolution of both the WD data and the SWH data is 0.25°, while the spatial resolution of SST data is 0.2°.

B. Data Preprocessing

To ensure that the experimental results are not affected by low-quality observables, the CYGNSS observables undergo quality control and filtering based on established criteria [33], [34] as follows.
1) All negative values will be discarded.
2) Observables with an incidence angle less than 35° will be discarded.
3) Observables with range corrected gain value less than 5 will be discarded.
4) Observables with poor overall quality will be discarded, indicated by the quality_flags.

After data filtering, the CYGNSS data was spatiotemporally matched with other datasets. The matching criteria for CYGNSS with NCEP, ERA5, CMC, and SMAP data were a linear distance less than 12.5 km and a time difference less than 30 min [35], [36]. For CYGNSS and Argo data matching, the criteria were a linear distance less than 0.5° and a time difference less than two days [28].

III. RELATIONSHIP BETWEEN THE SEA SURFACE BRIGHTNESS TEMPERATURE VARIATIONS AND THE GNSS-R OBSERVABLES

Previous studies have shown that it is feasible to directly link the brightness temperature variations induced by the sea surface roughness to ground-based GNSS-R observables [25], [27]. This section will analyze the relationship between the spaceborne GNSS-R observables from CYGNSS and the sea surface brightness temperature.

The technique of GNSS-R ocean scatterometry samples the reflected signal over the glistening zone in both delay and frequency (or Doppler), which enables the creation of a delay-Doppler map (DDM). The DDM is strongly correlated with the sea surface roughness. A theoretical model has already been
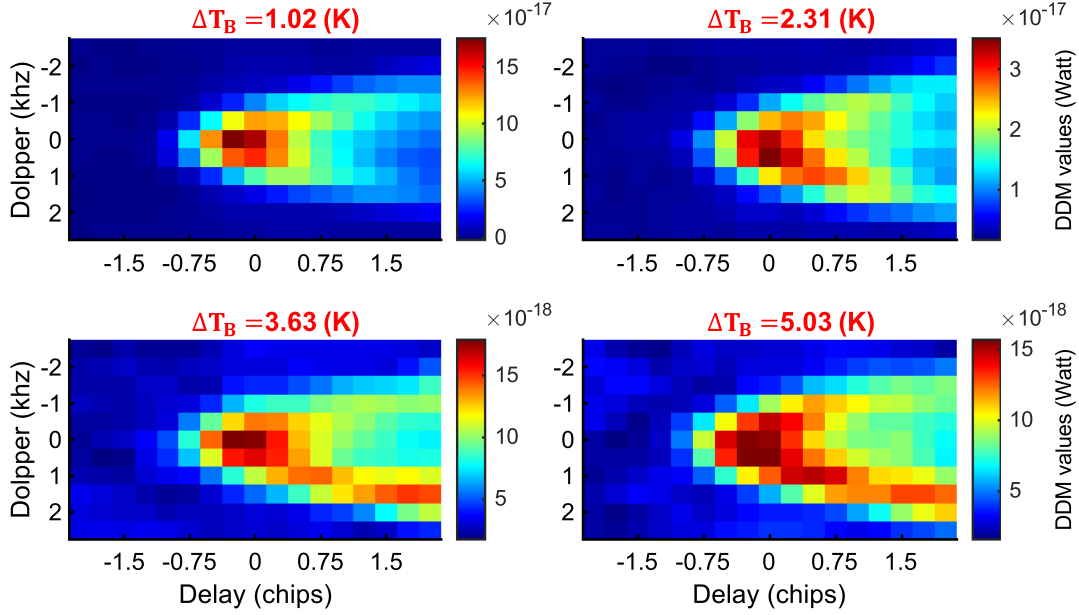
Fig. 1.   DDMs corresponding to different brightness temperature variations.

developed for the reflected GNSS signal as follows [14]:

$$\left\langle |Y(\tau,f)|^2 \right\rangle = \frac{P_t G_t \lambda^2 T_i^2}{(4\pi)^3} \iint_A \frac{G_r(r)\,\sigma_0 \Lambda^2(\tau)\,S^2(f)}{R_t^2 R_r^2} dA \tag{1}$$

where $\left\langle |Y(\tau,f)|^2 \right\rangle$ is the function of code delay (τ) and Doppler frequency (f), representing the DDM power. P_t is the transmitter power. G_t is the GNSS antenna gain. λ is the L-band wavelength. T_i is the coherent integration time. G_r is the receiver antenna gain. $\Lambda^2(\tau)$ is the delay code autorelation function. $S^2(f)$ is the Doppler frequency function. A is the glistening zone over the sea surface. R_t and R_r represent the distances from the transmitter and receiver, respectively, to the specular reflection point. σ_0 is the scattering parameter sensitive to sea surface roughness.

Fig. 1 shows the different brightness temperature variations and their corresponding DDM. As the brightness temperature variations increase, the power in the DDM becomes more scattered, and the maximum power gradually decreases. This indicates that DDM is directly related to brightness temperature variations. Therefore, in this study, some variables extracted from DDM that are closely related to brightness temperature variations will be used to correct brightness temperature and improve the accuracy of retrieval SSS.

Due to its sensitivity to sea surface roughness, normalized bistatic radar cross section (NBRCS) is strongly correlated with brightness temperature variations. NBRCS is calculated by summing the scattering cross sections $\bar{\sigma}_0$ and the effective scattering areas $\bar{A}_0$ on a bin-by-bin basis, as shown in the following equation:

$$\text{NBRCS} = \frac{\bar{\sigma}_0}{\bar{A}_0} = \frac{\sum_{i=1}^M \sum_{j=1}^N \bar{\sigma}_{\tau_i,f_j}}{\sum_{i=1}^M \sum_{j=1}^N \bar{A}_{\tau_i,f_j}} \tag{2}$$

where M and N represent the DDM bins for delay and Doppler, respectively, used in calculating both the scattering cross section

and effective scattering area DDMs. τ_i is the time delay. f_j is the frequency shift. $\bar{\sigma}_{\tau_i,f_j}$ and $\bar{A}_{\tau_i,f_j}$ represent the value of the bistatic radar cross section (BRCS) DDM bin and effective scattering area.

Similarly, the leading edge slope (LES) of the integrated delay waveform (IDW) within the 5 Doppler $\times$ 3 delay box is highly sensitive to the sea surface roughness. Expressions are as follows:

$$\begin{cases} \text{IDW}\ (\tau) = \frac{1}{N}\ \sum_{j=1}^N \left(DDM\left(\tau, f_j\right) \right)^2 \\ \text{LES} = \frac{M\sum_{i=1}^M \tau_i IDW_i - \sum_{i=1}^M \tau_i \sum_{i=1}^M \text{IDW}_i}{M\sum_{i=1}^M (\tau_i)^2 - \left(\sum_{i=1}^M \tau_i\right)^2} \end{cases} \tag{3}$$

In addition, the signal-to-noise ratio (SNR) of the DDM is also used in this study to correct brightness temperature, which is defined as

$$\text{SNR} = 10\log_{10}\left(\frac{S_{\max} - N_{\text{avg}}}{N_{\text{avg}}}\right) \tag{4}$$

where $S_{\max}$ is the maximum value (in raw counts) in a single DDM bin and N_{avg} is the average per-bin raw noise counts.

Fig. 2 shows the correlation between the brightness temperature variations and the CYGNSS observables. To enhance the visualization of the relationship between CYGNSS observables and brightness temperature variations, we used the logarithm of CYGNSS observables [lg (CYGNSS observables)]. The red dashed lines are the fitted lines, all intersecting the warm-color region (where the majority of samples are clustered). CYGNSS observables show a moderate negative correlation with the brightness temperature variations, with NBRCS being the most sensitive to the brightness temperature variations, followed by LES, and SNR being the least sensitive. Compared with the vertical brightness temperature variation (V–ΔTB), the horizontal brightness temperature variation (H–ΔTB) shows a stronger correlation with CYGNSS observables. This result is consistent
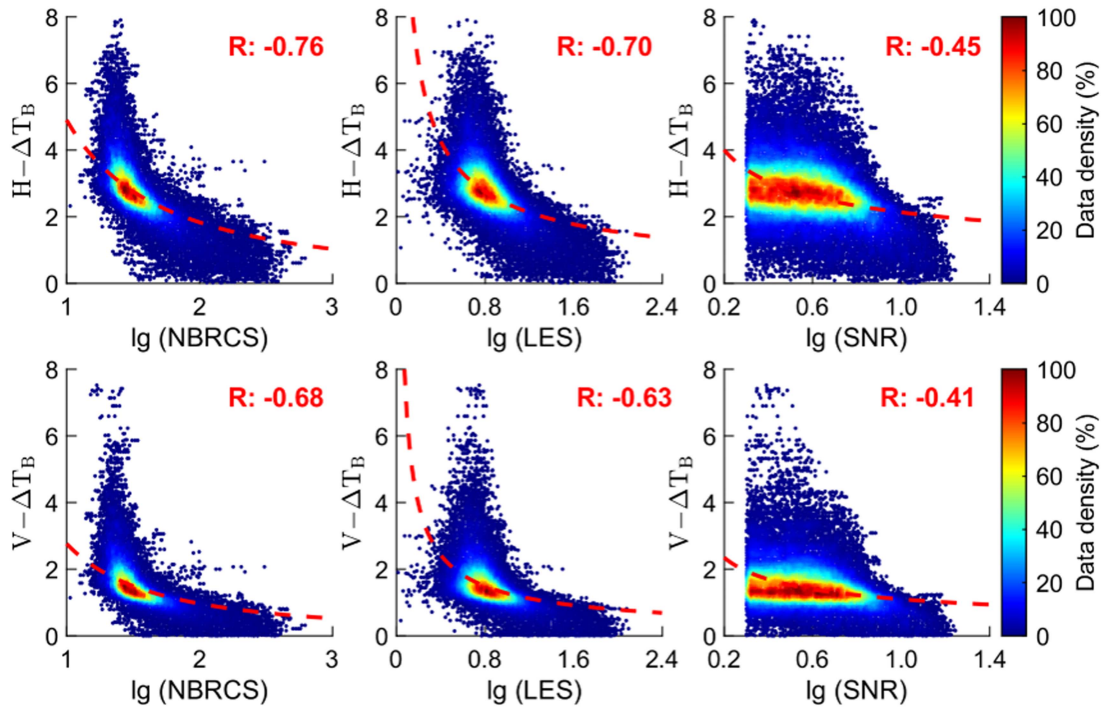
Fig. 2. Brightness temperature variations with corresponding CYGNSS observables, R denotes the correlation coefficient between them.
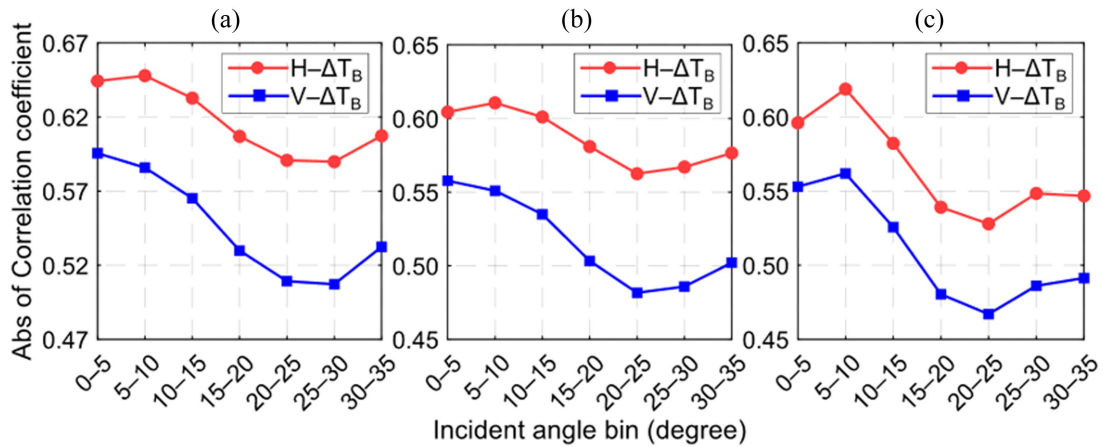

Fig. 3. Correlation coefficient between CYGNSS observables and brightness temperature variations at different incidence angles bins. (a) NBRCS. (b) LES. (c) SNR.

with the findings from the ground-based experiments, indicating that horizontal brightness temperature variation has a greater impact on GNSS-R observables [27].

Fig. 3 shows the sensitivity of CYGNSS observables to brightness temperature variations at different incidence angles (θ) bins. Data were sorted into seven incidence angle bins. To ensure result accuracy, 150 000 samples were uniformly sampled from each bin, mitigating the impact of uneven sample distribution on the outcomes. The illustration shows that the correlation coefficient between CYGNSS observables and brightness temperature variation reaches its highest point in most cases at incidence angles of 5°–10°, and reaches its lowest point at angles of 20°–25°. In addition, the general trend indicates a gradual

reduction in the correlation as the incidence angle increases, which implies a decrease in the sensitivity to brightness temperature variation.

Fig. 4 shows the relationship between the CYGNSS observables and the incidence angle after controlling for brightness temperature variations. Table I presents the correlation coefficients of the CYGNSS observables with the incidence angle. There is no significant correlation between NBRCS and incidence angle, whereas LES and SNR exhibit a degree of correlation with incidence angle. Upon controlling for brightness temperature variations, LES and SNR increase as the incidence angle rises, indicating the need to factor in the incidence angle when employing CYGNSS observables to retrieve SSS.
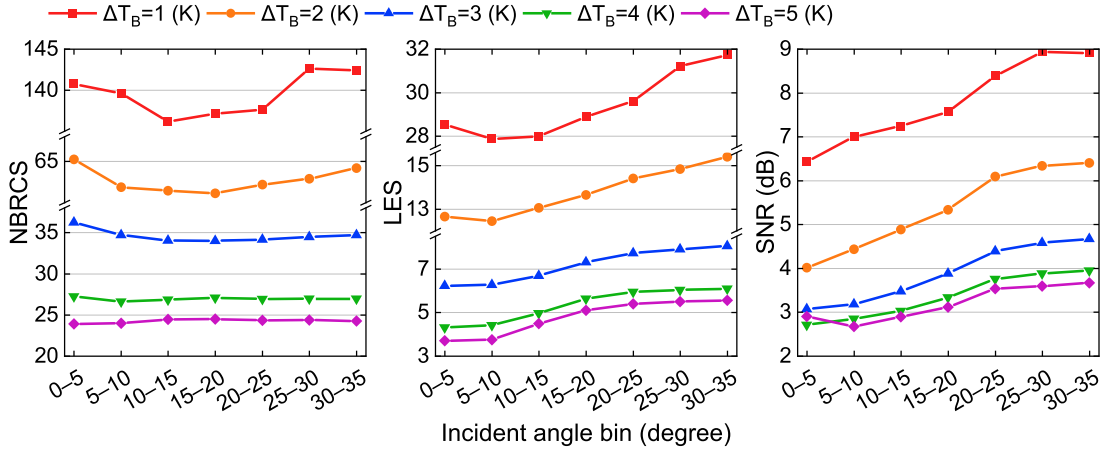
Fig. 4. CYGNSS observables for different incidence angle bins after controlling for brightness temperature variations.

TABLE I
CORRELATION COEFFICIENTS OF THE CYGNSS OBSERVABLES WITH THE INCIDENCE ANGLE

	NBRCS	LES	SNR
ΔT_B= 1 (K)	0.13	0.79	0.97
ΔT_B= 2 (K)	-0.18	0.94	0.98
ΔT_B= 3 (K)	-0.52	0.97	0.98
ΔT_B= 4 (K)	-0.15	0.94	0.98
ΔT_B= 5 (K)	0.12	0.92	0.92

IV. PERFORMANCE EVALUATION OF SMAP SSS RETRIEVAL WITH THE INCLUSION OF CYGNSS OBSERVABLES

In the SSS optimization of SMAP, the sea surface brightness temperature (T_B) is represented as the sum of the flat sea surface brightness temperature ($T_{B,falt}$) and the wind-induced brightness temperature difference ($\Delta T'_B$), which can be expressed as follows [31]:

$$T_B = T_{B,falt}\,(SSS, SST) + \Delta T'_B\,(WS, SWH, WD, SST)$$
(5)

where $T_{B,falt}$ is a function of SSS and SST, and $\Delta T'_B$ is a function of sea surface WS, SWH, WD, and SST. Therefore, after correcting the brightness temperature, SSS can be retrieved from the flat sea surface brightness temperature. SMAP retrieves SSS by a maximum likelihood algorithm with the following objective function [28]:

$$f(SSS, WS) = \sum_i \left[\frac{T_{B,i} - T^m_{B,i}\,(SSS, WS, SWH, WD, SST)}{NEDT_i}\right]^2$$
$$+ \left[\frac{WS - WS_{NCEP}}{\delta_{ws}}\right]^2$$
(6)

where i is one of the four flavors (i.e., H-aft, V-aft, H-fore, and V-fore). $T_{B,i}$ is SMAP L2A TB measurements at one of the four flavors. $T^m_{B,i}$ represents the modeled T_B in (5) as a function of SSS, SST, WS, SWH, and WD. NEDT is the noise-equivalent delta TB in SMAP L2A. WS_{NCEP} is ancillary WS, while δ_{ws} represents the a priori standard deviation on WS, with $\delta_{ws} = 1.5$ m/s.

Previous theoretical studies have indicated that sea surface brightness temperature variations arise from a combination of factors, including the sea surface wind field. Therefore, using wind field information to correct sea surface brightness temperature is unsatisfactory. On the other hand, GNSS-R measurements provide a direct response to sea surface roughness, and when combined with sea surface brightness temperature, they will significantly improve the retrieval of SSS [10].

Equation (6) demonstrates that the association between SSS and brightness temperature entails a complex interplay of multiple factors, rather than being a simple linear relationship. Although SSS can be retrieved from sea surface brightness temperature using geophysical model function (GMF), the results are not satisfactory.

Artificial neural networks (ANN) provide a powerful tool for solving complex nonlinear problems by extracting the underlying relationships hidden in large datasets through the process of learning from data. ANN achieves this by continuously adjusting the neural network parameters using the gradient descent method and error backpropagation, with the goal of minimizing the square error of the network [37], [38]. Mathematically, the forward-propagation principle can be represented as follows:

$$net_j = \sum_{I=0}^{N} W_{ij} X_i$$
(7)

where X_0 and W_{0j} denote the bias ($X_0 = 1$) and its corresponding bias weight, respectively. N is the number of input nodes. net_j denotes the input to the hidden node [39]. Multilayer perceptron (MLP) is one of the most commonly used ANN. We evaluated the retrieval performance of MLP models with different numbers of hidden layers and neurons, and the evaluation results are presented in Fig. 5. First, we set the number of neurons in each layer to 16 and evaluated the retrieval performance of the MLP model with 1 to 7 hidden layers, respectively. The results show that the retrieval performance is best when the MLP model has four hidden layers with an root mean square error (RMSE) of 0.65 psu. Subsequently, we evaluated the effect of different numbers of neurons on the retrieval performance. The
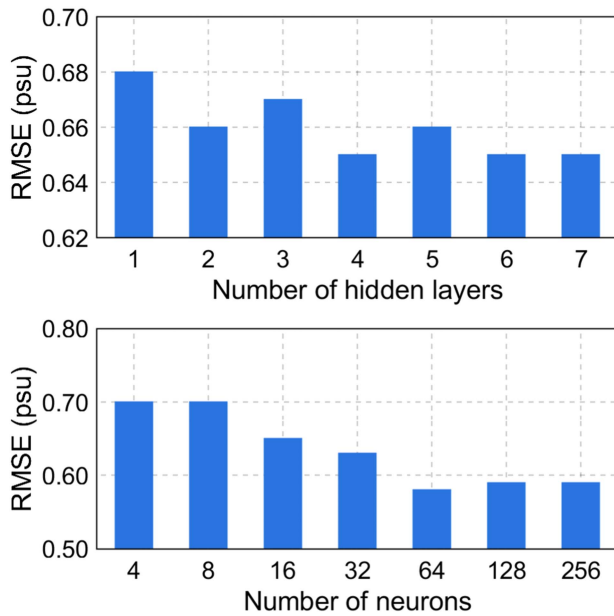
Fig. 5. SSS retrieval performance for different MLP network structures.

results show that the retrieval performance is optimal when the number of neurons is 64, with an RMSE of 0.58 psu. There was no improvement in retrieval performance when the number of neurons was increased to 128 and 256, both with an RMSE of 0.59 psu. Therefore, an MLP model with four hidden layers, each with 64 neurons, is used in this study to evaluate the performance of SSS retrieval for different data combinations. The experiment involved a total of 275 715 data points. The training dataset comprised 75% of the entire dataset, while the remaining 25% constituted the testing dataset. To facilitate a comprehensive comparison of the SSS retrieval method proposed, we also used the SSS performance obtained from SMAP as a reference. To evaluate the contribution of different parameters to SSS retrieval, we set up six cases and performed the corresponding SSS retrieval using MLP as follows.

Case 1: TB, WSNCEP, SWH, WD, SST.
Case 2: TB, WSCY, SWH, WD, SST.
Case 3: TB, NBRCS, θ, WD, SST.
Case 4: TB, LES, θ, WD, SST.
Case 5: TB, SNR, θ, WD, SST.
Case 6: TB, NBRCS, LES, SNR, θ, WD, SST.

The input parameters for Case 1 are the same as those for GMF (6) to evaluate the retrieval performance of GMF and MLP. In contrast, Case 2 uses WS data from CYGNSS L2 level version 3.1 data instead of WS data from NCEP. CYGNSS L1 level observables (NBRCS, LES, and SNR) were used to replace the sea surface wind field information (WS and SWH) in Cases 3–5, respectively. These three CYGNSS L1 level observables are used simultaneously in Case 6 to replace the sea surface wind field information. The specific experimental process of this study is shown in Fig. 6.

Fig. 7 displays the SSS retrieval performance for various cases. All retrieval results based on MLP showed better retrieval performance compared with the SSS provided by SMAP. This is attributable to the greater complexity and accuracy of the MLP model used in the retrieval process compared with SMAP's GMF. This can be more intuitively verified by comparing the retrieval performance of SMAP and Case 1, as they use the same input variables. The RMSE of SSS retrieved by SMAP is 0.68 psu, and the RMSE of SSS retrieved by Case1 is 0.58 psu. The replacement of NCEP WS data with L2-level WS data from CYGNSS in Case 2 resulted in a degraded SSS retrieval performance. The RMSE of the retrieval results increased from 0.58 to 0.62 psu, and the correlation coefficient (R) decreased from 0.83 to 0.81. These findings indicate that WS data from CYGNSS L2 level version 3.1 data have slightly inferior performance compared to those from NCEP. The experimental groups that utilized CYGNSS L1 observables (Cases 3–6) exhibited better retrieval performance compared with the experimental groups that used WS and SWH (Cases 1 and 2). This confirms the prior hypothesis that GNSS-R observables can better correct brightness temperature variations and improves the retrieval performance of SSS [10]. The simultaneous use of NBRCS, LES, and SNR to retrieve SSS further improved the retrieval performance. The RMSE decreased to 0.46 psu, while the R increased to 0.90 (Cases–5 versus Case 6).

Fig. 8 presents a scatter plot that compares retrieved SSS with Argo SSS. In this study, Cases 3–6 all utilized CYGNSS observables combined with SMAP for salinity retrieval. Therefore, only the best-performing Case 6 results will be discussed in the following text. The scatter plot illustrates that the GMF-based SMAP retrieval results typically underestimate salinity at low salinities (<35 psu) and overestimate salinity at high salinities ($>= 35$ psu). In contrast, MLP-based retrieval overestimates salinities at low salinities and underestimates salinities at high salinities. Fig. 9 shows that GMF-based SMAP retrieval errors are mostly positive (red) in most regions, with only a few low-salinity areas exhibiting negative errors (blue). MLP-based retrieval errors are mainly negative in high-salinity areas and positive in low-salinity areas. Combining CYGNSS observables significantly reduces retrieval errors. Compared to other methods, Case 6 exhibits better retrieval performance, with more data points symmetrically distributed along the y = x line and fewer scattered around it. Retrieval errors are also closer to zero, indicating higher stability and reliability.

Fig. 10 illustrates the correlation between SSS retrieval error and WS. It can be observed that the error gradually decreases with increasing WS as long as the WS remains below 4 m/s. The limited impact of WS on brightness temperature variations under low WS conditions is the probable cause of this phenomenon. This leads to inadequate contribution of wind field information to SSS retrieval [9], [28], [40]. With increasing WS, there is an increase in the sensitivity of brightness temperature variations to the wind field. Between WS of 4 and 12 m/s, the retrieval error remains relatively stable and is lower than that under low WS (<4 m/s). While WS exceed 12 m/s, the wind field still has an effect on brightness temperature variations. However, the introduction of increased sea foam can lead to new uncertainties in SSS retrieval. Moreover, the accuracy of wind field information provided by weather models starts to deteriorate with increasing
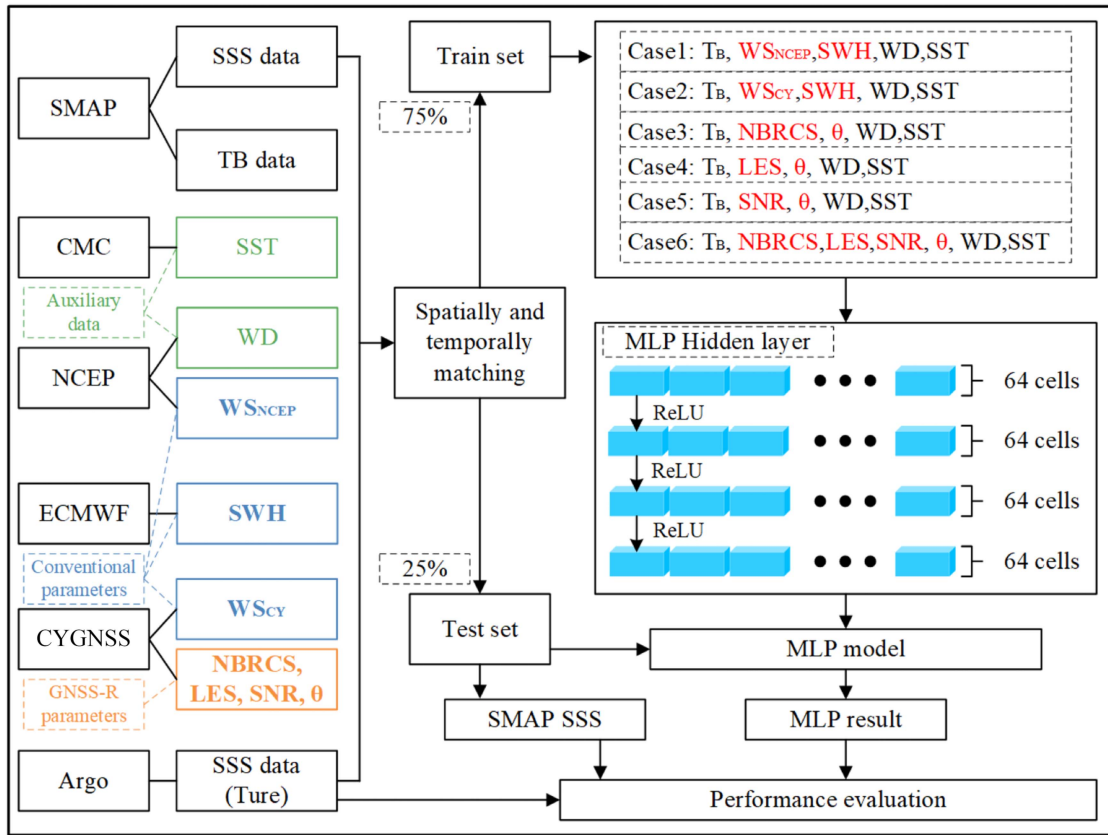
Fig. 6.   Experimental structure and process of this study.
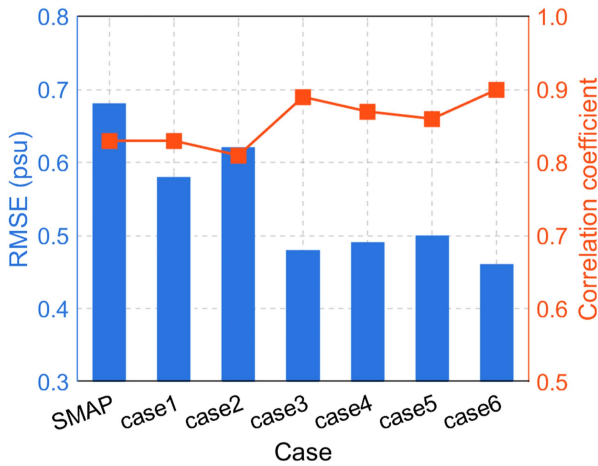

Fig. 7.   SSS retrieval performance of different cases.

WS. This results in higher SSS retrieval errors. Compared with wind field information, CYGNSS observables significantly improve the retrieval performance of SSS, especially in moderate to low WS, providing strong support for SSS retrieval. However, at high WS, the quality of CYGNSS observables deteriorates faster than that of reanalyzed wind field data fused with multiple sources, which is more stable in terms of data quality. Thus, the use of CYGNSS observables to improve the SSS retrieval performance under high WS conditions is limited.

V. DISCUSSION

While using CYGNSS L1 level observables can effectively correct for surface brightness temperature variations and provide support for SSS retrieval, there are still some issues that need to be further analyzed and resolved. As shown in Fig. 8, when the SSS is low (<33 psu), all methods exhibit large errors. This may be due to the fact that most of the low SSS is located in coastal areas (as illustrated by the Argo SSS distribution map in Fig. 9), where both SMAP observations and CYGNSS observations are affected by land contamination, resulting in large retrieval errors. Therefore, mitigating the impact of land contamination on observations is key to improving the performance of SSS retrieval in the future.

In addition, rainfall, as a common natural phenomenon at the sea surface, not only desalinates the salinity of seawater, but also causes changes in the roughness of the sea surface [41]. Although CYGNSS observables can provide some response to rainfall-induced roughness changes, this response is limited. Existing studies have shown that rainfall causes a reduction in the sea surface scattering cross-section, which affects the GNSS-R observations. However, this effect can only be observed when the sea surface WS up to 15 m/s [42], [43]. This may mean that CYGNSS is not able to respond accurately to rainfall-induced roughness changes at higher WS. Therefore, more research is needed in the future to improve the sensitivity of CYGNSS observables to sea surface roughness in order to more accurately
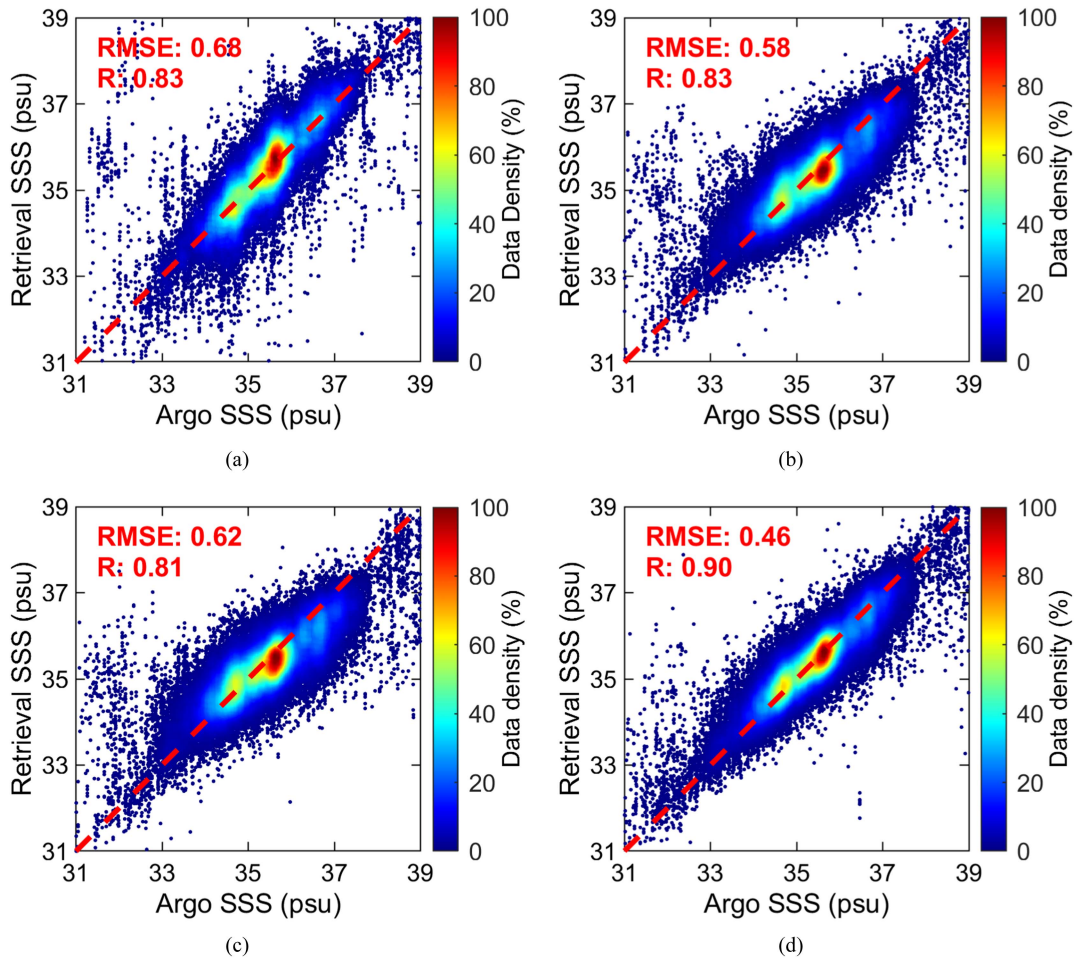
Fig. 8.   Density plots of SSS retrievals against Argo SSS for different cases. (a) is SMAP, (b) is Case 1, (c) is Case 2, (d) is Case 6.
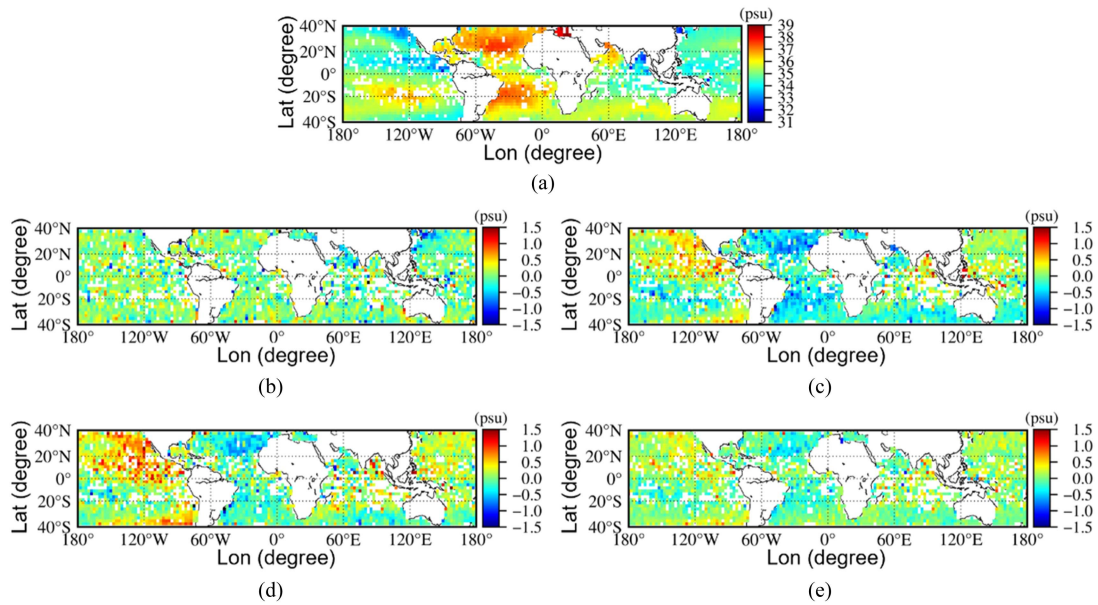

Fig. 9.   Argo SSS and retrieval bias distributions. (a) is Argo SSS, (b) is Bias of SMAP, (c) is Bias of Case 1, (d) is Bias of Case 2, (e) is Bias of Case 6.
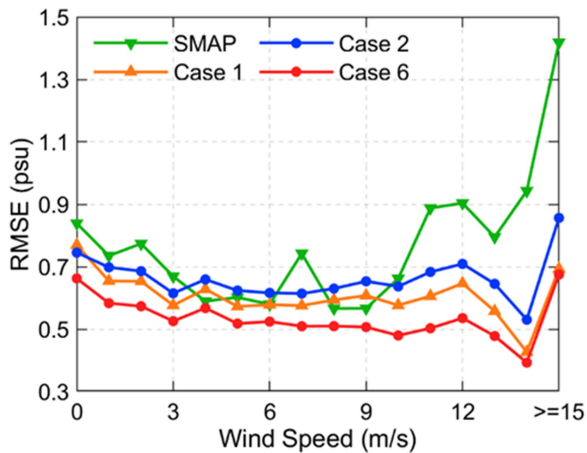
Fig. 10. RMSE of SSS retrievals at different WS.

correct brightness temperature variations caused by complex sea states.

VI. CONCLUSION

The traditional method for retrieving SSS typically corrects sea surface brightness temperature using wind field information. However, this method may produce suboptimal results because brightness temperature variations are influenced by factors beyond the wind field. Ground-based experiments have confirmed that GNSS-R observables directly respond to sea surface roughness and can be used to correct sea surface brightness temperature. However, there have been no experiments on retrieving SSS using joint L-band radiometer and spaceborne GNSS-R observational data. Therefore, the objective of this study is to assess the feasibility of utilizing CYGNSS observables to assist SMAP in SSS retrieval, and analyze the retrieval performance.

In this article, an MLP model is employed to verify the performance of SSS retrieval by SMAP brightness temperature combining different parameters. After controlling for brightness temperature variation, it is observed that LES and SNR in CYGNSS observations exhibit a moderate correlation with incidence angle. Therefore, the incidence angle of observations should be considered during SSS retrieval. The results demonstrate that the MLP-based SSS retrieval outperforms the GMF-based retrieval when using the same parameters, with the RMSE of retrieved salinity decreasing from 0.68 to 0.58 psu. However, the performance of using CYGNSS L2-level WS data in SSS retrieval is poor when compared to NCEP WS data. The RMSE increases from 0.58 to 0.62 psu. This is due to the slightly lower accuracy of CYGNSS WS data compared with NCEP. However, when using SMAP in combination with CYGNSS observables for SSS retrieval, the performance reaches its optimal level, with the RMSE of 0.46 psu and the R is 0.90. This finding indicates that CYGNSS observables are better at correcting sea surface brightness temperature and improving the retrieval performance of SSS compared with wind and wave information. This result is consistent with the assumption made in previous research [10].

Although the utilization of CYGNSS observables can enhance SSS retrieval performance. However, the limited quality of these observables still restricts the performance under high WS conditions. Thus, there is a need for further improvement in the performance of CYGNSS observables, along with appropriate quality control measures for observables at high WS. In addition, CYGNSS observables can only support SSS retrieval at middle and low latitudes, and there are currently insufficient GNSS-R observables to assist in SSS retrieval at high latitudes. Therefore, it is necessary to add spaceborne GNSS-R missions to address this issue.

REFERENCES

[1] J. E. Salisbury and B. F. Jönsson, "Rapid warming and salinity changes in the Gulf of Maine alter surface ocean carbonate parameters and hide ocean acidification," *Biogeochemistry*, vol. 141, pp. 401–418, Dec. 2018, doi: 10.1007/s10533-018-0505-3.

[2] Y. - C. Liang et al., "Amplified seasonal cycle in hydroclimate over the amazon river basin and its plume region.," *Nature Commun.*, vol. 11, Sep. 2020, Art. no. 4390, doi: 10.1038/s41467-020-18187-0.

[3] S. Hosoda, T. Ohira, and T. Nakamura, "A monthly mean dataset of global oceanic temperature and salinity derived from argo float observations," *JAMSTEC Rep. Res. Develop.*, vol. 21, pp. 47–59, Jan. 2008, doi: 10.5918/jamstecr.8.47.

[4] J. Font, G. S. E. Lagerloef, D. M. Le Vine, A. Camps, and O. - Z. Zanife, "The determination of surface salinity with the European SMOS space mission," *IEEE Trans. Geosci. Remote Sens.*, vol. 42, no. 10, pp. 2196–2205, Oct. 2004, doi: 10.1109/tgrs.2004.834649.

[5] D. Entekhabi et al., "The soil moisture active passive (SMAP) mission," *Proc. IEEE*, vol. 98, no. 5, pp. 704–716, May 2010, doi: 10.1109/jproc.2010.2043918.

[6] A. G. Fore, S. H. Yueh, W. Tang, B. W. Stiles, and A. K. Hayashi, "Combined active/passive retrievals of ocean vector wind and sea surface salinity with SMAP," *IEEE Trans. Geosci. Remote Sens.*, vol. 54, no. 12, pp. 7396–7404, Dec. 2016, doi: 10.1109/tgrs.2016.2601486.

[7] X. Yin, J. Boutin, E. Dinnat, Q. Song, and A. Martin, "Roughness and foam signature on SMOS-MIRAS brightness temperatures: A semi-theoretical approach," *Remote Sens. Environ.*, vol. 180, pp. 221–233, Jul. 2016, doi: 10.1016/j.rse.2016.02.005.

[8] G. Lagerloef et al., "The aquarius/SAC-D mission: Designed to meet the salinity remote-sensing challenge," *Oceanography*, vol. 21, no. 1, pp. 68–81, Mar. 2008, doi: 10.5670/oceanog.2008.68.

[9] A. Camps et al., "The WISE 2000 and 2001 field experiments in support of the SMOS mission: Sea surface L-band brightness temperature observations and their application to sea surface salinity retrieval," *IEEE Trans. Geosci. Remote Sens.*, vol. 42, no. 4, pp. 804–823, Apr. 2004, doi: 10.1109/tgrs.2003.819444.

[10] J. F. Marchan-Hernandez, N. Rodriguez-Alvarez, A. Camps, X. Bosch-Lluis, I. Ramos-Perez, and E. Valencia, "Correction of the sea state impact in the L-band brightness temperature by means of delay-Doppler maps of global navigation satellite signals reflected over the sea surface," *IEEE Trans. Geosci. Remote Sens.*, vol. 46, no. 10, pp. 2914–2923, Oct. 2008.

[11] S. H. Yueh et al., "L-band passive and active microwave geophysical model functions of ocean surface winds and applications to aquarius retrieval," *IEEE Trans. Geosci. Remote Sens.*, vol. 51, no. 9, pp. 4619–4632, Sep. 2013, doi: 10.1109/tgrs.2013.2266915.

[12] C. D. Hall and R. A. Cordey, "Multistatic scatterometry," *Int. Geosci. Remote Sens. Symp., Int. Geosci. Remote Sens. Symp.*, vol. 9, Jan. 1988, Art. no. 4251.

[13] M. Martin-Neira, "A pasive reflectometry and interferometry system (PARIS) application to ocean altimetry," *ESA J.*, vol. 31, Jan. 1993, Art. no. 254852.

[14] V. U. Zavorotny and A. G. Voronovich, "Scattering of GPS signals from the ocean with wind remote sensing application," *IEEE Trans. Geosci. Remote Sens.*, vol. 32, no. 2, pp. 951–964, Mar. 2000, doi: 10.1109/36.841977.

[15] Y. Pan, C. Ren, Y. Liang, Z. Zhang, and Y. Shi, "Inversion of surface vegetation water content based on GNSS-IR and MODIS data fusion," *Satell. Navigation*, vol. 1, no. 1, Dec. 2020, Art. no. 21, doi: 10.1186/s43020-020-00021-z.

[16] M. P. Clarizia, C. S. Ruf, P. Jales, and C. Gommenginger, "Spaceborne GNSS-R minimum variance wind speed estimator," *IEEE Trans. Geosci. Remote Sens.*, vol. 52, no. 11, pp. 6829–6843, Nov. 2014, doi: 10.1109/tgrs.2014.2303831.

[17] Z. Li, F. Guo, F. Chen, Z. Zhang, and X. Zhang, "Wind speed retrieval using GNSS-R technique with geographic partitioning," *Satell. Navigation*, vol. 4, no. 1, Dec. 2023, Art. no. 35, doi: 10.1186/s43020-022-00093-z.

[18] Q. Peng and S. Jin, "Significant wave height estimation from space-borne cyclone-GNSS reflectometry," *Remote Sens.*, vol. 11, no. 5, Mar. 2019, Art. no. 584, doi: 10.3390/rs11050584.

[19] C. Wang, K. Yu, K. Zhang, J. Bu, and F. Qu, "Significant wave height retrieval based on multi-variable regression models developed with CYGNSS data," *IEEE Trans. Geosci. Remote Sens.*, vol. 61, 2020, Art. no. 4200415.

[20] A. Alonso Arroyo et al., "Dual-polarization GNSS-R interference pattern technique for soil moisture mapping," *IEEE J. Sel. Topics Appl. Earth Observ. Remote Sens.*, vol. 7, no. 5, pp. 1533–1544, May 2014, doi: 10.1109/jstars.2014.2320792.

[21] C. C. Chew and E. E. Small, "Soil moisture sensing using spaceborne GNSS reflections: Comparison of CYGNSS reflectivity to SMAP soil moisture," *Geophysical Res. Lett.*, vol. 45, no. 9, pp. 4049–4057, May 2018, doi: 10.1029/2018gl077905.

[22] A. Rius, J. M. Aparicio, E. Cardellach, M. Martín-Neira, and B. Chapron, "Sea surface state measured using GPS reflected signals," *Geophysical Res. Lett.*, vol. 29, no. 23, pp. 37–31–37–4, Dec. 2002, doi: 10.1029/2002gl015524.

[23] A. Rius, J. M. Aparicio, E. Cardellach, M. Martín-Neira, and B. Chapron, "Sea surface state measured using GPS reflected signals," *Geophysical Res. Lett.*, vol. 9, pp. 37–31–37–4, Dec. 2002, doi: 10.1029/2002gl015524.

[24] A. Camps, "Passive advanced unit (PAU): A hybrid L-band radiometer, GNSS-reflectometer and IR-radiometer for passive remote sensing of the ocean," in *Proc. IEEE Int. Geosci. Remote Sens. Symp.*, 2007, pp. 2901–2904.

[25] E. Valencia et al., "Experimental relationship between the sea brightness temperature changes and the GNSS-R delay-doppler maps: Preliminary results of the ALBATROSS field experiments," in *Proc. IEEE Int. Geosci. Remote Sens. Symp.*, 2009, pp. III–741–III–744, doi: 10.1109/igarss.2009.5417871.

[26] J. F. Marchan-Hernandez et al., "Sea-state determination using GNSS-R data," *IEEE Geosci. Remote Sens. Lett.*, vol. 7, no. 4, pp. 621–625, Oct. 2010, doi: 10.1109/lgrs.2010.2043213.

[27] E. Valencia et al., "On the use of GNSS-R data to correct L-band brightness temperatures for sea-state effects: Results of the ALBATROSS field experiments," *IEEE Trans. Geosci. Remote Sens.*, vol. 49, no. 9, pp. 3225–3235, Sep. 2011, doi: 10.1109/tgrs.2011.2159224.

[28] B. Liu et al., "First assessment of CyGNSS-incorporated SMAP sea surface salinity retrieval over pan-tropical ocean," *IEEE J. Sel. Topics Appl. Earth Observ. Remote Sens.*, vol. 14, pp. 12163–12173, 2021, doi: 10.1109/jstars.2021.3128553.

[29] C. S. Ruf et al., "New ocean winds satellite mission to probe hurricanes and tropical convection," *Bull. Amer. Meteorological Soc.*, vol. 97, no. 3, pp. 385–395, Mar. 2016, doi: 10.1175/bams-d-14-00218.1.

[30] C. Ruf et al., "In-orbit performance of the constellation of CYGNSS hurricane satellites," *Bull. Amer. Meteorological Soc.*, vol. 100, no. 10, pp. 2009–2023, Oct. 2019, doi: 10.1175/bams-d-18-0337.1.

[31] T. Meissner, F. J. Wentz, A. Manaster, R. Lindsley, M. Brewer, and M. Densberger, *Remote Sensing Systems SMAP Ocean Surface Salinities [Level 2C, Level 3 Running 8- day, Level 3 Monthly], Version 5.0 validated release. Remote Sensing Systems*, Santa Rosa, CA, USA, 2022. [Online]. Available: www.remss.com/missions/smap

[32] E. Oka and K. Ando, "Stability of temperature and conductivity sensors of argo profiling floats," *J. Oceanogr.*, vol. 60, no. 2, pp. 253–258, Jan. 2004, doi: 10.1023/b:joce.0000038331.10108.79.

[33] C. S. Ruf and R. Balasubramaniam, "Development of the CYGNSS geophysical model function for wind speed," *IEEE J. Sel. Topics Appl. Earth Observ. Remote Sens.*, vol. 12, no. 1, pp. 66–77, Jan. 2019.

[34] M. Asgarimehr, C. Arnold, T. Weigel, C. Ruf, and J. Wickert, "GNSS reflectometry global ocean wind speed using deep learning: Development and assessment of CyGNSSnet," *Remote Sens. Environ.*, vol. 269, Feb. 2022, Art. no. 112801, doi: 10.1016/j.rse.2021.112801.

[35] X. Li et al., "Analysis of coastal wind speed retrieval from CYGNSS mission using artificial neural network," *Remote Sens. Environ.*, vol. 260, Jul. 2021, Art. no. 112454, doi: 10.1016/j.rse.2021.112454.

[36] F. Chen, X. Zhang, F. Guo, J. Zheng, Y. Nan, and M. Freeshah, "TDS-1 GNSS reflectometry wind geophysical model function response to GPS block types," *Geo-Spatial Inf. Sci.*, vol. 25, no. 2, pp. 312–324, Apr. 2022, doi: 10.1080/10095020.2021.1997076.

[37] J. Reynolds, M. P. Clarizia, and E. Santi, "Wind speed estimation from CYGNSS using artificial neural networks," *IEEE J. Sel. Topics Appl. Earth Observ. Remote Sens.*, vol. 13, pp. 708–716, 2020, doi: 10.1109/jstars.2020.2968156.

[38] C. Lu, Z. Wang, Z. Wu, Y. Zheng, and Y. Liu, "Global ocean wind speed retrieval from GNSS reflectometry using CNN-LSTM network," *IEEE Trans. Geosci. Remote Sens.*, vol. 61, 2023, Art. no. 5801112, doi: 10.1109/TGRS.2023.3276173.

[39] B. Rani, K. Srinivas, and A. Govardhan, "Rainfall prediction with TLBO optimized ANN," *J. Sci. Ind. Res.*, vol. 73, pp. 643–647, 2014.

[40] T. Meissner, F. J. Wentz, and L. Ricciardulli, "The emission and scattering of L-band microwave radiation from rough ocean surfaces and wind speed measurements from the aquarius sensor," *J. Geophysical Res.: Oceans*, vol. 119, no. 9, pp. 6499–6522, Sep. 2014, doi: 10.1002/2014jc009837.

[41] M. Asgarimehr et al., "Remote sensing of precipitation using reflected GNSS signals: Response analysis of polarimetric observations," *IEEE Trans. Geosci. Remote Sens.*, vol. 60, Jan. 2022, Art. no. 5800412, doi: 10.1109/tgrs.2021.3062492.

[42] J. Bu, K. Yu, S. Han, N. Qian, Y. Lin, and J. Wang, "Retrieval of sea surface rainfall intensity using spaceborne GNSS-R data," *IEEE Trans. Geosci. Remote Sens.*, vol. 60, Jan. 2022, Art. no. 5803116, doi: 10.1109/tgrs.2022.3168928.

[43] R. Balasubramaniam and C. Ruf, "Characterization of rain impact on L-band GNSS-R ocean surface measurements," *Remote Sens. Environ.*, vol. 239, Mar. 2020, Art. no. 111607, doi: 10.1016/j.rse.2019.111607.

Zheng Li received the B.Sc. and M.Sc. degrees in survey engineering from Xi'an University of Science and Technology, Xi'an, China, in 2018 and 2021, respectively. He is currently working toward the Ph.D. candidate with distinction in geodesy at Wuhan University, Wuhan, China.

His current research focuses on GNSS reflectometry.
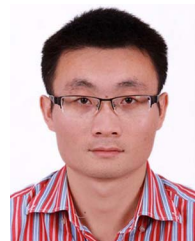
Fei Guo received the B.Sc. degree in survey engineering from Nanjing Forestry University, Nanjing, China, in 2007, and the M.Sc. and Ph.D. degrees with distinction in geodesy from Wuhan University, Wuhan, China, in 2009 and 2013, respectively.

He is currently a Professor with the School of Geodesy and Geomatics, Wuhan University. His current research mainly focuses on GNSS precise positioning and its application in geoscience.

Zhiyu Zhang received the M.Sc. degree in navigation, guidance and control in 2020 from Wuhan University, Wuhan, China, where he is currently workinh toward the Ph.D. candidate with distinction in geodesy at Wuhan University.

His current research focuses on GNSS remote sensing.

Xiaohong Zhang received the B.Sc., M.Sc. and Ph.D. degrees with distinction in geodesy and engineering surveying from Wuhan University, Wuhan, China, in 1997, 1999, and 2002, respectively.

He is currently a Professor with Wuhan University. His main research interests include PPP, PPP-RTK, GNSS/INS integration technology and its applications.